

1 **Pharmacological rescue of impaired mitophagy in Parkinson's disease-related LRRK2**
2 **G2019S knock-in mice**

3 Francois Singh¹, Alan R. Prescott², Graeme Ball², Alastair D. Reith³, and Ian G. Ganley^{1*}

4 ¹ MRC Protein Phosphorylation and Ubiquitylation Unit, University of Dundee, Dundee DD1 5EH, UK

5 ² Dundee Imaging Facility, School of Life Sciences, University of Dundee, Dundee DD1 5EH, UK

6 ³Novel Human Genetics Research Unit, GlaxoSmithKline Pharmaceuticals R&D, Stevenage, UK

7 * **Address for correspondence: i.ganley@dundee.ac.uk**

8 Running Title: LRRK2 regulated mitophagy

9 Key Words: Parkinson's, LRRK2, mitophagy, autophagy, kinase inhibitor, GSK3357679A

10

11 **Abstract**

12 Parkinson's disease (PD) is a major and progressive neurodegenerative disorder, yet the
13 biological mechanisms involved in its aetiology are poorly understood. Evidence links this
14 disorder with mitochondrial dysfunction and/or impaired lysosomal degradation – key features
15 of the autophagy of mitochondria, known as mitophagy. Here we investigated the role of
16 LRRK2, a protein kinase frequently mutated in PD, on this process *in vivo*. Using mitophagy
17 and autophagy reporter mice, bearing either knockout of LRRK2 or expressing the pathogenic
18 kinase-activating G2019S LRRK2 mutation, we found that basal mitophagy was specifically
19 altered in clinically relevant cells and tissues. Our data show that basal mitophagy inversely
20 correlates with LRRK2 kinase activity *in vivo*. In support of this, use of distinct LRRK2 kinase
21 inhibitors in cells increased basal mitophagy, and a CNS penetrant LRRK2 kinase inhibitor,
22 GSK3357679A, rescued the mitophagy defects observed in LRRK2 G2019S mice. This study
23 provides the first *in vivo* evidence that pathogenic LRRK2 directly impairs basal mitophagy, a
24 process with strong links to idiopathic Parkinson's disease, and demonstrates that
25 pharmacological inhibition of LRRK2 is a rational mitophagy-rescue approach and potential
26 PD therapy.

27

28 **Introduction**

29 Parkinson's disease (PD) is the second most common neurodegenerative disorder, affecting 1-
30 2% of the population over 60 years old, and 4% above 85 years of age ¹. The main symptoms
31 of PD are muscle rigidity, bradykinesia, resting tremor, and postural instability and may be
32 accompanied by sleep disorders, anosmia, depression, and dementia ². It is characterised by a
33 progressive and selective degeneration of dopaminergic (DA) neurons of the substantia nigra
34 pars compacta (SNpc). Currently, there are no treatments available that modify the course of
35 neurodegenerative decline. Although this disease is mostly sporadic, about 15% of cases appear
36 to be inherited and in support of this, 20 genes implicated in PD have been identified from
37 familial genetic studies while ~90 loci have been identified from PD-GWAS ³. The exact causes
38 of PD are currently unknown but some evidence strongly links impaired mitochondrial and
39 lysosomal function to disease pathology ².

40 Mutations in *PARK8*, encoding for LRRK2 (Leucine Rich Repeat Kinase 2), are the most
41 frequently reported cause of PD ⁴. The most common mutation associated with PD is the
42 substitution of glycine at position 2019 of LRRK2 to serine (G2019S), representing 4% of
43 familial and 1% of sporadic cases ⁵. LRRK2 is a large multidomain protein with two catalytic
44 domains: a Ras of complex (ROC) GTPase domain that is able to bind GTP and hydrolyse it,
45 and a kinase domain that utilises a subset of Rab GTPases as substrates ⁶. Importantly, all the
46 segregating mutations associated with PD are located in the catalytic core. A mutation in the
47 ROC/COR domain, such as the R1441C/G/H or the Y1699C mutation, leads to decreased
48 GTPase activity and elevated kinase activity ⁷. Mutations in the kinase domain, such as the
49 G2019S or the I2020T, also lead to an elevated kinase activity. Hence, enhanced kinase activity
50 appears to be a common factor in pathogenic LRRK2 mutations. Although the function of

51 LRRK2 within cells is currently unknown, mounting evidence implicates a role in membrane
52 trafficking ^{6,8,9}.

53 Macroautophagy is a membrane trafficking pathway that delivers intracellular components to
54 the lysosome for degradation ¹⁰. These components can include whole organelles such as
55 mitochondria. The autophagic turnover of mitochondria is termed mitophagy, which acts as a
56 mitochondrial quality control mechanism that allows the selective degradation of damaged or
57 unnecessary mitochondria ^{11,12}. Mitophagy itself has strong links to PD following the landmark
58 discoveries that PINK1 and Parkin, two other genes mutated in familial PD, sequentially
59 operate to initiate mitophagy in response to mitochondrial depolarisation in cell lines ¹³⁻¹⁶.
60 However, when this pathway becomes relevant *in vivo*, and under what physiological
61 conditions, is unclear especially given that PINK1 and Parkin are not required for regulation of
62 mitophagy under normal, or basal, conditions ¹⁷⁻¹⁹. Indeed, our understanding of the detailed
63 mechanisms regulating basal mitophagy remains elusive.

64 In this study, we sought to define the physiological link between mitochondrial turnover and
65 LRRK2 in relation to PD. We utilised our previously published mouse reporter models to study
66 mitophagy (*mito-QC*) and autophagy (*auto-QC*; Fig. 1A, C and ^{17,20,21}) in either LRRK2
67 knockout mice, or knock-in mice harbouring the pathogenic LRRK2 G2019S mutation. Whilst
68 we found minimal impact of LRRK2 on general autophagy (macroautophagy), we observed
69 that the LRRK2 G2019S activation-mutation was associated with reduced mitophagy in
70 specific tissues, including dopaminergic neurons and microglia within the brain. In contrast,
71 knockout of LRRK2 resulted in increased mitophagy. Taken together, these data imply that
72 LRRK2 kinase activity inversely correlates with basal mitophagy levels. In support of this, we
73 found that that treatment of cells or animals with the potent and selective CNS penetrant
74 LRRK2 kinase inhibitor, GSK3357679A (Ding et al., in preparation), rescued these LRRK2

75 G2019S-associated mitophagy defects and enhanced mitophagy in dopamine neurons and
76 microglia in the brains of genotypically normal mice. Our results identify a physiological role
77 for LRRK2 in the regulation of basal mitophagy *in vivo* and underline the potential value of
78 pharmacological inhibition of LRRK2 as a potential therapeutic strategy to ameliorate aspects
79 of Parkinson's disease driven by mitochondrial dysfunction.

80

81 **Material and methods**

82 *Animals*

83 Experiments were performed on mice genetically altered for Leucine-rich repeat kinase 2
84 (LRRK2), using either wild-type, LRRK2 G2019S⁶ mutation knock-in mice, or mice in which
85 LRRK2 has been ablated^{22,23} (KO). The mitophagy (*mito-QC*) and the autophagy (*auto-QC*)
86 reporter mouse models used in this study were generated as previously described^{17,20}.

87 *Primary mouse embryonic fibroblasts culture*

88 Primary mouse embryonic fibroblasts (MEFs) were derived, from time-mated pregnant females
89 at E12.5. Primary MEFs were maintained in DMEM (Gibco, 11960-044) supplemented with
90 10% FBS, 2 mM L-Glutamine (Gibco, 2503-081), 1% Na-Pyruvate (Gibco, 11360-070), 1%
91 Non-essential amino acids (Gibco, 11140-035), 1% Antibiotics (Penicillin/Streptomycin 100
92 U/ml penicillin and 100 µg/ml streptomycin; Gibco), and 150µM β-Mercaptoethanol (Gibco,
93 21985-023) at 37°C under a humidified 5% CO₂ atmosphere.

94 *Primary mouse embryonic fibroblasts treatments*

95 To assess mitophagy and autophagy upon stimulation, cells were treated for 24 hours with
96 either 1 mM 3-Hydroxy-1,2-dimethyl-4(1H)-pyridone (Deferiprone/DFP, Sigma-Aldrich,
97 379409), or incubated in Earl's balanced salt solution (EBSS, Gibco, 24010-043). *mito-QC*
98 MEFs were also treated for 24 hours with LRRK2 kinase activity inhibitors GSK2578215A²⁴
99 (250, 500, 1000 nM), MLi-2²⁵ (5, 10, and 20 nM), or GSK3357679A (compound **39**, Ding et
100 al., in prep.) (0.1, 1, 10, 100, 1000 nM). All treatments (apart from EBSS) were in DMEM
101 (Gibco, 11960-044) supplemented with 10% FBS, 2 mM L-Glutamine (Gibco, 2503-081), 1%
102 Non-essential amino acids (Gibco, 11140-035), 1% Antibiotics (Penicillin/Streptomycin 100

103 U/ml penicillin and 100 µg/ml streptomycin; Gibco), and 150µM β-Mercaptoethanol (Gibco,
104 21985-023) at 37°C under a humidified 5% CO₂ atmosphere. MLi-2 and GSK2578215A were
105 synthesized by Natalia Shapiro (University of Dundee) as described previously^{24,25}.

106 ***Light Microscopy***

107 MEFs were plated on glass coverslips and treated as described in the previous paragraph. At
108 the end of the treatment, cells were washed twice in DPBS (Gibco, 14190-094), and fixed in
109 3.7% Paraformaldehyde (Sigma, P6148), 200 mM HEPES, pH=7.00 for 20 minutes. Cells were
110 washed twice with, and then incubated for 10 minutes with DMEM, 10mM HEPES. After a
111 wash with DPBS, nuclei were stained with Hoechst 33342 (1 µg/mL, Thermo Scientific, 62249)
112 for 5 minutes. Cells were washed in DPBS and mounted on a slide (VWR, Superfrost, 631-
113 0909) with Prolong Diamond (Thermo Fisher Scientific, P36961). Images were acquired using
114 a Nikon Eclipse Ti-S fluorescence microscope with a 63x objective.

115 ***Quantitation of Mitophagy and Autophagy in vitro***

116 Quantification of red-only dots was semi-automatized using the *mito-QC* counter plugin on
117 FIJI as previously described^{26,27}. Autophagosomes and autolysosomes were quantified using
118 the Autophagy counter plugin on FIJI developed in house, following the same principle as the
119 *mito-QC* counter²⁸. The macro “auto-QC_counter.ijm” (“version 1.0 release”, DOI:
120 10.5281/zenodo.4158361) is available from the following github repository:
121 https://github.com/graemeball/auto-QC_counter.

122 ***Animal Studies***

123 Experiments were performed on 81 adult mice (9-23 weeks old) of both genders (n=8-12 per
124 group for the mito-QC reporter, and n=9-15 per group for the auto-QC reporter), all
125 homozygous for the corresponding reporter (mitophagy or autophagy).

126 The effect of the CNS penetrant LRRK2 kinase inhibitor GSK3357679A *in vivo* was assessed
127 using 50 adult mice (9-17 weeks old at the end of the study), all homozygous for the mito-QC
128 reporter. Mice of both genders were randomly assigned to the vehicle or to the GSK3357679A
129 treated group (WT-Vehicle: n=10, WT-GSK3357679A: n=10, G2019S-Vehicle: n=10,
130 G2019S-GSK3357679A: n=10, KO-Vehicle: n=5, and KO-GSK3357679A: n=5). Vehicle
131 treated animals were dosed (10 mL/kg) with aqueous methylcellulose (1% w/v, Sigma, M0512)
132 prepared in sterile water (Baxter, UKF7114), or with GSK3357679A (15 mg/kg/dose) prepared
133 in aqueous methylcellulose. Treatment was administered by oral gavage every 12 hours for a
134 total of four times per mouse. Mice were culled 2 hours (+/- 9 minutes) after the last dosing.

135 Animals were housed in sex-matched littermate groups of between two and five animals per
136 cage in neutral temperature environment ($21^{\circ} \pm 1^{\circ}\text{C}$), with a relative humidity of 55-65%, on
137 a 12:12 hour photoperiod, and were provided food and water *ad libitum*. All animal studies
138 were ethically reviewed and carried out in accordance with Animals (Scientific Procedures) Act
139 1986 as well as the GSK Policy on the Care, Welfare and Treatment of Animals, and were
140 performed in agreement with the guidelines from Directive 2010/63/EU of the European
141 Parliament on the protection of animals used for scientific purposes. All animal studies and
142 breeding were approved by the University of Dundee ethical review committee, and further
143 subjected to approved study plans by the Named Veterinary Surgeon and Compliance Officer
144 (Dr. Ngairé Dennison) and performed under a UK Home Office project license in agreement
145 with the Animal Scientific Procedures Act (ASPA, 1986).

146 ***Sample collection***

147 Mice were terminally anaesthetised with an intraperitoneal injection of pentobarbital sodium
148 (Euthatal, Merial) then trans-cardially perfused with DPBS (Gibco, 14190-094) to remove
149 blood. Tissues were collected and either snap frozen in liquid nitrogen and stored at -80°C for
150 later biochemical analyses or processed by overnight immersion in freshly prepared fixative:
151 3.7% Paraformaldehyde (Sigma, P6148), 200 mM HEPES, pH=7.00. The next day, fixed
152 tissues were washed three times in DPBS, and immersed in a sucrose 30% (w/v) solution
153 containing 0.04% sodium azide until they sank at the bottom of the tube. Samples were stored
154 at 4°C in that sucrose solution until further processing.

155

156 *Immunolabeling of brain free-floating sections*

157 The brain was frozen-sectioned axially using a sledge microtome (Leica, SM2010R), and 50
158 microns thick sections were stored in PBS at 4°C until further treatment. Free-floating sections
159 were permeabilised using DPBS (Gibco, 14190-094) containing 0.3% Triton X-100 (Sigma
160 Aldrich, T8787) 3 times for 5 minutes. Sections were then blocked for one hour in blocking
161 solution (DPBS containing 10% goat serum (Sigma Aldrich, G9023), and 0.3% Triton X-100).
162 Primary antibody incubation was performed overnight in blocking solution containing one of
163 the following antibodies: Anti-Tyrosine Hydroxylase (1/1000, Millipore, AB152), Anti-Iba-1
164 (1/1000, Wako, 019-19741), Anti Calbindin-D28k (1/1000, Swant, CB38), Anti-Glial
165 Fibrillary Acidic Protein (1/1000, Millipore, MAB360). The next day, sections were washed 2
166 times for 8 minutes in DPBS containing 0.3% Triton X100 and then incubated for 1 hour in
167 blocking solution containing the secondary antibody (1/200, Invitrogen P10994 Goat anti-
168 Rabbit IgG (H+L) Cross-Adsorbed Secondary Antibody, Pacific Blue, or Invitrogen P3182
169 Goat anti-Mouse IgG (H+L) Cross-Adsorbed Secondary Antibody, Pacific Blue). Sections
170 were then washed 2 times for 8 minutes in DPBS containing 0.3% Triton X100 and mounted

171 on slides (Leica Surgipath® X-tra™ Adhesive, 3800202) using Vectashield Antifade Mounting
172 Medium (Vector Laboratories, H-1000) and sealed with nail polish.

173 ***Tissue section and immunostaining***

174 Tissues were embedded in an O.C.T. compound matrix (Scigen, 4586), frozen and sectioned
175 with a cryostat (Leica CM1860UV). 12 microns sections were placed on slides (Leica
176 Surgipath® X-tra™ Adhesive, 3800202), and then air dried and kept at -80°C until further
177 processing. Sections were thawed at room temperature and washed 3 times 5 minutes in DPBS
178 (Gibco, 14190-094). Sections were then counterstained for 5 minutes with Hoechst 33342
179 (1µg/mL, Thermo Scientific, 62249). Slides were mounted using Vectashield Antifade
180 Mounting Medium (Vector Laboratories, H-1000) and high precision cover glasses (No. 1.5H,
181 Marienfeld, 0107222) and sealed with transparent nail polish.

182 ***Confocal microscopy***

183 Confocal micrographs were obtained by uniform random sampling using either a Zeiss
184 LSM880 with Airyscan, or a Zeiss 710 laser scanning confocal microscope (Plan-Apochromat
185 63x/1.4 Oil DIC M27) using the optimal parameters for acquisition (Nyquist). 10-15 images
186 were acquired per sample, depending on the tissue, by an experimenter blind to all conditions.
187 High resolution, representative images were obtained using the Super Resolution mode of the
188 Zeiss LSM880 with Airyscan.

189 ***Quantitation of Mitophagy and Autophagy in vivo***

190 Quantification of mitophagy and autophagy was carried out on at least 10 pictures per
191 sample. Images were processed with Volocity Software (version 6.3, Perkin-Elmer). Images
192 were first filtered using a fine filter to suppress noise. Tissue was detected by thresholding the

193 Green channel. For the immunolabelings in the brain (TH, Iba1, Calbindin D-28k, and GFAP),
194 each cell population of interest was detected by thresholding the Pacific Blue labelled channel.
195 A ratio image of the Red/Green channels was then created for each image.
196 For the mito-QC reporter, mitolysosomes were then detected by thresholding the ratio channel
197 as objects with a high Red/Green ratio value within the tissue/cell population of interest. The
198 same ratio channel threshold was used per organ/set of experiments. To avoid the detection of
199 unspecific high ratio pixels in the areas of low reporter expression, a second red threshold was
200 applied to these high ratio pixels. This double thresholding method provides a reliable detection
201 of mitolysosomes as structures with a high Red/Green ratio value and a high Red intensity
202 value.

203 For the general autophagy reporter, high intensity red pixels were detected by thresholding the
204 red channel within the tissue/cell population of interest. The same red channel threshold was
205 used per organ/set of experiments. Autophagosomes and autolysosomes were then
206 differentiated by thresholding the high intensity red pixels depending on their Red/Green ratio
207 channel value. Pixels with a low Red/Green ratio were considered as autophagosomes, whereas
208 pixels with a high Red/Green ratio were considered as autolysosomes. The same ratio channel
209 threshold was used per organ/set of experiments.

210 *Filipin staining*

211 Frozen fixed tissue sections were washed in PBS to remove any excess O.C.T compound
212 (Scigen, 4586) excess. Sections were then incubated for 2 hours at room temperature with filipin
213 (200 µg/mL; Sigma-Aldrich, F9765) and then washed twice in PBS. Tissue sections were
214 mounted using Vectashield Antifade Mounting Medium (Vector Laboratories, H-1000) and
215 sealed with nail polish. High resolution, representative images were obtained using the Super

216 Resolution mode of the Zeiss LSM880 with Airyscan (Plan-Apochromat 63x/1.4 Oil DIC
217 M27).

218

219 *Western blotting*

220 Frozen tissue was homogenized with a Cellcrusher™ (Cellcrusher, Cork, Ireland) tissue
221 pulveriser. Approximately 20-30 mg of pulverised tissue were then lysed on ice for 30 min with
222 (10 µL/mg tissue) of RIPA buffer [50 mM Tris-HCl pH 8, 150 mM NaCl, 1 mM EDTA, 1%
223 NP-40, 1% Na-deoxycholate, 0.1% SDS, and cOmplete™ protease inhibitor cocktail (Roche,
224 Basel, Switzerland)], phosphatase inhibitor cocktail (1.15 mM sodium molybdate, 4 mM
225 sodium tartrate dihydrate, 10 mM β-glycerophosphoric acid disodium salt pentahydrate, 1 mM
226 sodium fluoride, and 1mM activated sodium orthovanadate), and 10 mM DTT. After lysis, the
227 mixture was vortexed and centrifuged for 10 min at 4 °C at 20,817 G. The supernatant was
228 collected, and the protein concentration determined using the Pierce BCA protein assay kit
229 (ThermoFisher Scientific, Waltham, MA, USA). For each sample, 20-25 µg of protein was
230 separated on a NuPAGE 4–12% Bis-Tris gel (Life technologies, Carlsbad, CA, USA). Proteins
231 were electroblotted to 0.45µm PVDF membranes (Imobilon-P, Merck Millipore, IPVH00010;
232 or Amersham Hybond, GE Healthcare Life Science, 10600023), and immunodetected using
233 primary antibodies directed against phospho-Ser935 LRRK2 rabbit monoclonal (1/1000, MRC
234 PPU Reagents and Services, UDD2), LRRK2 rabbit monoclonal (1/1000, MRC PPU Reagents
235 and Services, UDD3), phospho-Rab10 (Thr73) rabbit monoclonal (1/1000, Abcam, ab230261),
236 Rab10 mouse monoclonal (1/1000, nanoTools 0680-100/Rab10-605B11), α-Tubulin (11H10)
237 Rabbit monoclonal antibody (1/10000, CST, 2125S), and β-Actin mouse monoclonal antibody
238 (1/1000, Proteintech, 60008-1-Ig). All antibodies to LRRK2 were generated by MRC PPU
239 Reagents and Services, University of Dundee (<http://mrcppureagents.dundee.ac.uk>).

240 ***Statistics***

241 Data are represented as means \pm SEM. Number of subjects are indicated in the respective figure
242 legends. Statistical analyses were performed using a one-way analysis of variance (ANOVA)
243 or two-way ANOVA followed by a Tukey HSD using RStudio version 1.1.1335²⁹. Statistical
244 significance is displayed as * $p < 0.05$; ** $p < 0.01$, *** $p < 0.001$, and **** $p < 0.0001$.

245

246 **Results**

247 ***The pathogenic G2019S LRRK2 mutation impairs basal mitophagy but not autophagy in*** 248 ***vitro***

249 To investigate the physiological role of LRRK2 in regulating autophagy we utilised two
250 previously validated and highly similar mouse reporter models^{17,20,21}. These transgenic reporter
251 models rely on constitutive expression of a tandem mCherry-GFP tag from the *Rosa26* locus.
252 In the *mito-QC* model, which monitors mitophagy, the tandem tag is localised to mitochondria
253 (by an outer mitochondrial targeting sequence derived from residues 101-152 of the protein
254 FIS1). In the *auto-QC* model, which monitors general (macro)autophagy, the tandem tag is
255 localised to autophagosomes (by conjugation to the N-terminus of MAP1LC3b). For both
256 models, when a mitochondrion or autophagosome is delivered to lysosomes, the low lysosomal
257 luminal pH is sufficient to quench the GFP signal, but not that from mCherry. Hence, the degree
258 of mitophagy or general autophagy can be determined by the appearance of mCherry-only
259 puncta, which represent mito/autolysosomes (Fig. 1A and D). Given that mitophagy is a form
260 of autophagy, the use of both models allows us to monitor the specificity of autophagy *in vivo*.
261 A large disruption of autophagy in general will also influence mitophagy, whereas a block in
262 mitophagy, which likely represents a small fraction of the total autophagy occurring at any one
263 time, will tend to have little influence on the total autophagic levels.

264 To investigate the effect of LRRK2 kinase activity on mitophagy, we first isolated and
265 cultured primary mouse embryonic fibroblasts (MEFs) derived from wild type mice (WT), mice
266 homozygous for the Parkinson's disease-associated LRRK2 G2019S mutant, or mice
267 homozygous for a LRRK2 knockout (KO) variant; all of which were on a homozygous *mito-*
268 *QC* reporter background (Fig. 1B and C). A small degree of basal mitophagy was evident in all
269 cell lines. However, we observed that LRRK2 G2019S KI mutant cells displayed significantly

270 lower basal mitophagy levels, whereas the absence of LRRK2 (KO) led to an increase of this
271 process. Interestingly, our data suggests that LRRK2 predominantly influences basal mitophagy
272 as deferiprone (DFP), a strong mitophagy inducer³⁰, increased mitophagy to a similar level
273 across all genotypes (Fig. S1A and B).

274 We next investigated general autophagy using the LRRK2 mouse lines mentioned above
275 on the homozygous *auto*-QC background. In contrast to mitophagy, in isolated primary MEFs
276 we noticed no significant difference in the number of mCherry-only autolysosomes across all
277 the *Lrrk2* genotypes under basal conditions (Fig. 1E and F). We also analysed amino acid
278 starvation-induced autophagy, by incubation in Earls Balanced Salt Solution (EBSS). A robust
279 autophagy response was observed in all cells and as with basal autophagy, the *Lrrk2* genotype
280 failed to significantly alter this large increase in autolysosomes (Fig. S1C).

281 ***LRRK2 kinase inhibitors correct the G2019S mitophagy defects in vitro***

282 Using genetics, our observations show that LRRK2 kinase activity inversely correlates
283 with mitophagy *in vitro*. If this is the case, then pharmacological inhibition of LRRK2 kinase
284 activity should also increase mitophagy. Therefore, we aimed to investigate if the mitophagy
285 deficit observed in the G2019S cells could be rescued with LRRK2-selective kinase inhibitors.
286 To that end, we first studied the effect of two structurally distinct tool LRRK2 kinase inhibitors,
287 GSK2578215A²⁴ and MLi-2²⁵, in primary *mito*-QC MEFs. In the WT group, treatment of cells
288 for 24 h with either compound increased mitophagy to values comparable to what we previously
289 observed in the LRRK2 KO group (Fig. S1D). Although MLi-2 is a more potent LRRK2 kinase
290 inhibitor (IC₅₀ 0.76 nM²⁵) compared to GSK2578215A (IC₅₀ 10nM²⁴), at higher concentrations
291 it did not stimulate mitophagy. In the G2019S group, significantly higher concentrations of
292 GSK2578215A were necessary to stimulate mitophagy and this may reflect the increased kinase
293 activity of this mutant³¹. However, with MLi-2 we were not able to fully rescue the mitophagy

294 defect. As with the WT cells, treatment with MLi-2 at the highest dose (20 nM) did not stimulate
295 mitophagy. The failure of higher doses of MLi-2 to stimulate mitophagy may be due to an off-
296 target effect, as at 20 nM it also inhibited mitophagy in the LRRK2 KO cells (Fig. S1D).
297 Therefore, we recommend caution when using MLi-2 at high concentrations. Neither
298 compound increased mitophagy in KO cells, demonstrating that their mitophagy-enhancing
299 properties are dependent on LRRK2. Additionally, both compounds inhibited LRRK2 activity,
300 as indicated by loss of LRRK2 S935 phosphorylation (an indirect measure of LRRK2 activity
301 ³², Fig. S1E).

302 With respect to mitophagy, the relatively low potency of GSK2578215A and the off-
303 target effects of MLi2, indicated the need for improved LRRK2 tool inhibitors. For this reason,
304 we turned to GSK3357679A, a novel pyrrolopyrimidine LRRK2 kinase inhibitor that exhibits
305 excellent cellular potency, selectivity, oral bioavailability and PK/PD correlation in animal
306 studies (Ding et al., in prep.). We tested GSK3357679A in primary *mito*-QC MEFs and
307 observed a dose-dependent effect on mitophagy with a maximal stimulation achieved at a
308 concentration of 10 nM in WT cells (Fig. 1G and H). In the G2019S cells we observed a reduced
309 response, with a maximal effect on mitophagy reached at 100 nM. Importantly, contrary to what
310 we observed with MLi-2, GSK3357679A effects on restoration of mitophagy were maintained
311 at the highest concentration used and exhibited no deleterious effects on mitophagy at any
312 concentration in LRRK2 KO cells. Western blotting analysis revealed that GSK3357679A
313 potently inhibited LRRK2 kinase activity in a dose-dependent manner, as indicated by
314 decreased phosphorylation of its substrate Rab10 at threonine 73 ⁶, as well as reduced LRRK2
315 S935 phosphorylation (Fig. 1H). Thus, genetically and chemically, the data show that LRRK2
316 inhibition enhances basal mitophagy in cells, and GSK3357679A displayed a superior
317 performance compared to other available LRRK2 kinase inhibitors.

318 ***Mutation of LRRK2 in vivo alters mitophagy in specific cell populations within the brain***

319 Given the effects of LRRK2 kinase activity on mitophagy *in vitro*, we next sought to
320 use our mouse lines to investigate this *in vivo*. PD is primarily a neurodegenerative disorder, so
321 we first explored mitophagy in the brain. We focussed on four cell populations: two neuronal
322 populations linked to movement - dopaminergic (DA) neurons of the substantia nigra pars
323 compacta (SNpc) and Purkinje neurons of the cerebellum; as well as in two glial cell
324 populations - cortical microglia and cortical astrocytes. In midbrain, we identified SNpc DA
325 neurons using tyrosine hydroxylase (TH) staining and found no difference in the number of DA
326 neurons per field across the *Lrrk2* genotypes (Fig. 2A and B). These cells are the mouse
327 equivalent of the human population of DA neurons that degenerate in PD and we had previously
328 found that they undergo substantial mitophagy¹⁷. Basal mitophagy was enhanced in the LRRK2
329 KO neurons compared to the WT, and although not statistically significant, mitophagy appeared
330 reduced in DA neurons of LRRK2 G2019S KI mice compared to WT (Fig. 2A and C). This
331 was similar to our earlier observations in MEFs and showed that the presence of LRRK2 can
332 impact mitophagy in this clinically relevant population of neurons within the midbrain. To
333 determine if this effect is typical of neurons in general, we investigated mitophagy in another
334 neuronal population involved in motor control, the Purkinje neurons. These cells were
335 identified in cerebellar sections using immunostaining against the calcium sensor Calbindin-
336 D28k. These cells are rich in mitochondria and as shown previously²⁰, they also undergo
337 significant mitophagy (Fig. 2D). Contrary to what we observed in SNpc DA neurons, no
338 statistical difference in mitophagy in Purkinje cells was found between any group (Fig. 2E).

339 As we observed neuron-specific alterations of mitophagy, we next examined the effect
340 of *Lrrk2* genotype in two distinct populations glial cells within the cortex. Immune-related
341 microglia were identified by Iba1 (ionized calcium-binding adapter molecule 1, Fig. 2F).

342 Interestingly, we observed an enhanced presence of microglial cells in the cortex of G2019S
343 animals when compared to WT or KO mice (Fig. 2G). We do not yet understand the nature of
344 this increase and further work will be needed to determine if there are simply more microglia
345 in the G2019S mice, or an increased movement of cells to this area of the brain. Regardless,
346 when normalised for cell number, we found a significant decrease in basal mitophagy in
347 G2019S microglia compared to WT, as well as an increase in mitophagy levels in KO cells
348 (Fig. 2H). Thus, as with DA neurons, LRRK2 can impacts basal mitophagy in microglia. In
349 contrast, cortical astrocytes, stained with glial fibrillary acidic protein (GFAP, Fig. 2I), did not
350 show any observable difference in mitophagy across *Lrrk2* genotypes (Fig. 2J).

351 In contrast to the *Lrrk2* genotype effects on mitophagy in DA neurons and microglia,
352 analysis of *auto-QC* mouse brains indicated no change in general macroautophagy in these cell
353 types (Fig. S2). Thus, the LRRK2 G2019S mutation is not causing a major disruption in
354 neuronal autophagy but does influence basal mitophagy levels.

355

356 ***Mutation of LRRK2 in vivo also alters mitophagy in peripheral organs with high LRRK2*** 357 ***expression***

358 We next assessed mitophagy levels in the lungs, a tissue in which the levels of LRRK2
359 are known to be elevated^{33,34}. Basal mitophagy across the whole lung was evident in all
360 genotypes and in a similar fashion to MEFs, DA neurons and microglia, mitophagy was reduced
361 in G2019S mice and enhanced (over 2-fold relative to WT) in KO mice (Fig. 3A and B),
362 Consistent with this, mitochondrial content was decreased when comparing KO to G2019S
363 (although no significant increase of this parameter was detected compared to WT, see Fig.
364 S3A). As previously reported^{35,36}, we observed enlarged type II pneumocytes with large

365 vesicular-like structures in all the animals of the LRRK2 KO group that is attributable to the
366 accumulation of large lamellar bodies, which are secretory lysosomes responsible for surfactant
367 release. We confirmed the nature of these structures as enlarged lamellar bodies by filipin
368 staining lung sections for cholesterol, a component found in surfactant (Fig. S3B).

369 The tissue reported to have the highest LRRK2 expression is the kidney^{33,34}. We first
370 investigated mitophagy in the kidney cortex, where we had previously shown the proximal
371 tubules to be a major site of mammalian mitophagy²⁰. LRRK2-dependent mitophagy changes
372 in the kidney were much lower in magnitude compared to the lung, yet there was a small
373 decrease in G2019S-expressing tissue (Fig.3C and D). However, we do note that mitophagy is
374 10-fold higher in this region compared to lung, which may mask relatively small changes
375 conferred by *Lrrk2* genotypes.

376 We next studied *in vivo* genotype effects on autophagy, using the same conditions and
377 organs as for the *mito*-QC reporter. Consistent with brain and MEF data, no significant
378 difference in the number of autolysosomes was observed in the lungs of *auto*-QC reporter mice
379 (Fig. 3E and F). Again, enlarged type II pneumocytes were observed in LRRK2 KO animals
380 (Fig. 3E). Likewise, in the kidney cortex we did not detect an effect of *LRRK2* genotype on
381 autolysosomes (Fig. 3G and H). We also note that no major difference was seen in the number
382 of autophagosomes across both lung and kidney (Fig. S3C and D). Taken together, these data
383 suggest that the *Lrrk2* genotype does not majorly affect all autophagy pathways but
384 predominantly impacts basal mitophagy, both *in vitro* and *in vivo*.

385

386 ***GSK3357679A corrects the G2019S mitophagy defect in vivo***

387 We next sought to determine if we could pharmacologically rescue the observed mitophagy
388 defects *in vivo*. For this purpose, we utilised GSK3357679A - the pharmacodynamic
389 characteristics of which have been shown to be suitable for extended oral dosing studies in
390 rodents (Ding et al., in prep). We administered *mito*-QC WT, G2019S, and LRRK2 KO mice
391 with GSK3357679A *via* oral gavage every 12 h for a total of four dosings. During this period,
392 we observed no effect of GSK3357679A on body weight in any genotype (Fig. S4A). Tissues
393 were then harvested 2 h post the final dosing. We focussed our analyses on tissues where our
394 previous analyses of *Lrrk2* genotypic variants suggested a LRRK2-dependent role in
395 mitophagy, namely the lung and brain as well as the kidney.

396 LRRK2 inhibition was confirmed in lung, brain and kidney tissue lysates of GSK3357679A
397 dosed mice by immunoblotting of LRRK2 phospho-S935 and of Rab10 phospho-T73 (Fig. 4A).
398 In the brain, GSK3357679A decreased the phosphorylation of LRRK2 on S935 in both WT and
399 G2019S mice (Fig. 4A and B). However, we were not able to detect Rab10 phosphorylation in
400 this tissue, suggesting Rab phosphorylation is low or tightly regulated (results not shown).
401 Regardless, the loss of S935 phosphorylation on LRRK2 is consistent with kinase inhibition in
402 the brain. LRRK2 kinase inhibition was also observed in the lungs and kidneys of the same
403 animals, with GSK3357679A treated mice showing significant loss of both LRRK2 S935
404 phosphorylation and Rab 10 T73 phosphorylation (Fig. 4A and B).

405 In DA neurons of the SNpc, we found that treatment with GSK3357679A increased
406 mitophagy in both WT and G2019S KI mice. Consistent with earlier results, the vehicle dosed
407 G2019S group displayed significantly lower mitophagy compared to the vehicle- dosed WTs,
408 (Fig. 4C and D, compare with Fig. 2A and C). Importantly, treatment with GSK3357679A
409 restored G2019S mitophagy to base-line WT levels (Fig. 4C and D). No difference was

410 observable in the KO groups in presence of GSK3357679A, showing mitophagy effects are
411 through on-target LRRK2 inhibition.

412 As we had observed differences in cortical microglial mitophagy between genotypes,
413 we next investigated the effect of GSK3357679A treatment on this cell population.
414 GSK3357679A increased mitophagy in the cortical microglia in both WT and G2019S groups
415 (Fig. 4E and F). Consistently, GSK3357679A restored G2019S mitophagy levels to a value
416 similar to that observed in the control group (WT-V). Mitophagy was unaffected by
417 GSK3357679A in the KO groups, confirming GSK3357679A specificity on LRRK2 kinase
418 activity. As seen earlier (Fig. 2G), microglial cell numbers were increased in the cortex of
419 vehicle-treated G2019S mice compared with vehicle-treated WT mice (Fig. S4B). Interestingly,
420 GSK3357679A treatment recovered the increase in number of cortical microglia observed in
421 LRRK2 G2019S KI mice (Fig S4B), suggesting that LRRK2 kinase activity is a key contributor
422 to regulation of microglial numbers in this mouse line.

423 In the lungs we found that GSK3357679A increased mitophagy levels in both WT and G2019S
424 KI animals (Fig. 4C and 4D). Importantly, in the G2019S group, GSK3357679A elevated
425 mitophagy levels to a value similar to the WT Vehicle group, suggesting LRRK2-inhibition can
426 rescue the G2019S-mediated defect in mitophagy in lung also. As observed for other LRRK2
427 inhibitors we observed enlarged lamellar bodies in Type-II pneumocytes in the lungs of mice
428 treated with GSK3357679A, similar to that observed in LRRK2 KO mice (Fig. 3A) and to what
429 has been previously reported in the presence of LRRK2 kinase inhibitors^{25,35,37}. GSK3357679A
430 had no effect on mitophagy levels in the lungs of LRRK2 KO mice (Fig.4G). Consistent with
431 the genetics, in the kidney we found that GSK3357679A had a minimal effect on mitophagy
432 despite this organ exhibiting robust LRRK2 inhibition (Fig. S4B and C and Fig 4A). Though

433 as previously mentioned, the very high levels of mitophagy in this tissue could be masking any
434 subtle mitophagy increases.

435 Taken together these results show that a pathogenic mutation of LRRK2 impairs basal
436 mitophagy in cells and tissues. Importantly, this phenotype can be rescued by the use of LRRK2
437 kinase inhibitors.

438 **Discussion**

439 Our work reveals that LRRK2 kinase activity inversely correlates with basal mitophagy levels,
440 both *in vitro* and *in vivo* in specific cells and tissues. Strikingly, the mitophagy defects seemed
441 to be specific to certain cell types. Indeed, we observed different effects in two different
442 neuronal subpopulations and in two microglial subpopulations. More work is needed to
443 understand why mitophagy is more sensitive to LRRK2 kinase activity in these cells, but it may
444 help explain why DA neurons degenerate in PD. Interestingly, we found a higher mitochondrial
445 content in the soma of Purkinje neurons compared to DA neurons, indicative of a higher
446 oxidative metabolism in the former. In addition, mitophagy levels were much lower in the
447 Purkinje cells, implying an inverse correlation between oxidative metabolism and mitophagy,
448 similar to previous observations in different muscle subtypes²⁶. Speculatively, the higher basal
449 level of mitophagy in these DA neurons could be required to maintain oxidative metabolism in
450 light of their lower mitochondrial numbers, thus rendering them susceptible to defects affecting
451 mitophagy. Also of potential relevance, we observed a higher difference in mitophagy levels
452 between genotypes in the cortical microglia than in the DA neurons. Brain resident microglia
453 have been shown to have much higher LRRK2 levels and activity than neuronal populations,
454 which could have implications for disease aetiology³⁸.

455 The work presented here shows for the first time that pathogenic LRRK2 mutations can alter
456 basal mitophagy in clinically relevant cell populations *in vivo*. However, the extent to which
457 impaired mitophagy drives an individual's Parkinson's disease remains to be determined. We
458 and others have previously found that loss of PINK1 or Parkin activity does not significantly
459 alter basal mitophagy rates *in vivo*, despite a well characterised role for the PINK1/Parkin
460 pathway on depolarisation-induced mitophagy^{17,18,39}. This implies that the PINK1/Parkin
461 pathway drives mitophagy under distinct types of stress, in contrast to the basally regulated
462 LRRK2 pathway described here. Regardless, if loss of stress-induced PINK1/Parkin-dependent
463 mitophagy can lead to PD, then it is reasonable to assume that loss of LRRK2-regulated basal
464 mitophagy could also contribute. These data now imply that impaired mitophagy may be a
465 common theme in PD pathology.

466 Recent reports in other models support our conclusion of a role for LRRK2 in regulating
467 mitophagy. *In vitro* assays in patient derived fibroblasts bearing G2019S or R1441C LRRK2
468 variants are consistent with our *in vitro* cell assays and observations *in vivo*⁴⁰⁻⁴³.

469 The mechanism by which LRRK2 kinase activity regulates basal mitophagy is currently
470 unclear. LRRK2 has been shown to phosphorylate a subset of Rab GTPases⁶ and, given the
471 roles of Rabs in membrane trafficking, it is tempting to suggest that they may be key in
472 regulating this mitophagy pathway^{8,44}. It has been recently shown that lysosomal overload
473 stress induces translocation of Rab7L1 and LRRK2 to lysosomes⁴⁵. This leads to the activation
474 of LRRK2 and the stabilisation of Rab8 and Rab10 through phosphorylation. Another recent
475 study showed that LRRK2 mutations inhibit the mitochondrial localisation of Rab10⁴⁰.

476 We used two highly similar reporter models in primary MEFs and in mice to study general
477 autophagy and mitophagy. The use of both the *mito-QC* and the *auto-QC* reporters, in
478 combination with selective LRRK2 kinase inhibitors, provided evidence that LRRK2 kinase

479 activity affects mitophagy, rather than autophagy in general. The role of LRRK2 kinase activity
480 on autophagy has been previously investigated in several studies with inconclusive or
481 contradictory effects ^{36,46–51}. However, with our reporter systems, we cannot entirely exclude
482 that other selective autophagy pathways are affected. Additionally, total flux through the
483 autophagy pathway is likely to be much higher than the relative flux attributable to mitophagy,
484 and combined with the observed higher inter-individual variability with our autophagy reporter,
485 this makes it potentially more difficult to pick up small changes. For these reasons, it would be
486 unreasonable to entirely exclude the involvement of LRRK2 in general autophagy, although
487 our results lack support for this.

488 Our results show that three structurally distinct selective LRRK2 kinase inhibitors are active on
489 mitophagy in MEF cells, and that *in vivo* the tool compound GSK3357679A demonstrates
490 similar cell-specific effects in DA neurons and microglia within the brain. Importantly, use of
491 this inhibitor *in vitro* and *in vivo* supported our genetic data in suggesting that LRRK2 kinase
492 activity inversely correlates with the level of basal mitophagy. The fact that we could rescue
493 G2019S-impaired mitophagy in PD-relevant cell types, within the brain, provides an exciting
494 prospect that LRRK2 inhibitor-mediated correction of mitophagic defects in Parkinson's
495 patients could have therapeutic utility in the clinic. In addition, LRRK2 kinase activity
496 inhibitors could also provide a way to increase mitophagy in general, which could be beneficial
497 in idiopathic PD, or indeed, in other non-related conditions where increased clearance of
498 mitochondria could be beneficial, such as mitochondrial diseases.

499 Here we demonstrate, through both genetic manipulation and pharmacology, that the most
500 common mutation in PD impairs basal mitophagy in tissues and cells of clinical relevance. The
501 fact that we can rescue this genetic defect in mitophagy using LRRK2 inhibitors, holds promise
502 for future PD therapeutics.

503 **Acknowledgements**

504 We would like to acknowledge Paul Appleton at the Dundee Imaging Facility, Dundee. The
505 Zeiss LSM880 with Airyscan was supported by the ‘Wellcome Trust Multi-User Equipment
506 Grant’ [208401/Z/17/Z]. We would also like to acknowledge Dr Jin-Feng Zhao and Dr Thomas
507 McWilliams for their expert technical assistance. This work was funded by a grant from the
508 Medical Research Council, UK (IGG; MC_UU_00018/2) and GlaxoSmithKline plc. Requests
509 for provision of GSK3357679A should be directed to Alastair Reith (alastair.d.reith@gsk.com).

510 **Author contribution**

511 Conception and design were done by F.S., A.D.R. and I.G.G. Experiments were performed by
512 F.S. and A.R.P. Data analysis was carried out by F.S. The autophagy counter plugin for FIJI
513 was developed by G.B. and F.S. Drafting and revision of the manuscript was carried out by
514 F.S., A.D.R. and I.G.G. All authors received and approved the final document.

515

516

517 **References**

- 518 1. Coppedè, F. Genetics and Epigenetics of Parkinson's Disease. *Sci. World J.* **2012**, 1–12
519 (2012).
- 520 2. Sironi, L., Restelli, L. M., Tolnay, M., Neutzner, A. & Frank, S. Dysregulated
521 Interorganellar Crosstalk of Mitochondria in the Pathogenesis of Parkinson's Disease.
522 *Cells* **9**, 233 (2020).
- 523 3. Deng, H., Wang, P. & Jankovic, J. The genetics of Parkinson disease. *Ageing Res. Rev.*
524 **42**, 72–85 (2018).
- 525 4. Bouhouche, A. *et al.* LRRK2 G2019S Mutation: Prevalence and Clinical Features in
526 Moroccans with Parkinson's Disease. *Parkinsons. Dis.* **2017**, 2412486 (2017).
- 527 5. Lill, C. M. Genetics of Parkinson's disease. *Mol. Cell. Probes* **30**, 386–396 (2016).
- 528 6. Steger, M. *et al.* Phosphoproteomics reveals that Parkinson's disease kinase LRRK2
529 regulates a subset of Rab GTPases. *Elife* **5**, (2016).
- 530 7. Rudenko, I. N. & Cookson, M. R. Heterogeneity of Leucine-Rich Repeat Kinase 2
531 Mutations: Genetics, Mechanisms and Therapeutic Implications. *Neurotherapeutics* **11**,
532 738–750 (2014).
- 533 8. Pfeffer, S. R. LRRK2 and Rab GTPases. *Biochem. Soc. Trans.* **46**, 1707–1712 (2018).
- 534 9. Hur, E.-M., Jang, E.-H., Jeong, G. R. & Lee, B. D. LRRK2 and membrane trafficking:
535 nexus of Parkinson's disease. *BMB Rep.* **52**, 533–539 (2019).
- 536 10. Yu, L., Chen, Y. & Tooze, S. A. Autophagy pathway: Cellular and molecular
537 mechanisms. *Autophagy* **14**, 207–215 (2018).
- 538 11. Rodger, C. E., McWilliams, T. G. & Ganley, I. G. Mammalian mitophagy – from in
539 vitro molecules to in vivo models. *FEBS Journal* vol. 285 1185–1202 (2018).

- 540 12. Montava-Garriga, L. & Ganley, I. G. Outstanding Questions in Mitophagy: What We
541 Do and Do Not Know. *J. Mol. Biol.* **432**, 206–230 (2020).
- 542 13. Narendra, D., Tanaka, A., Suen, D. F. & Youle, R. J. Parkin is recruited selectively to
543 impaired mitochondria and promotes their autophagy. *J. Cell Biol.* **183**, 795–803
544 (2008).
- 545 14. Koyano, F. *et al.* Ubiquitin is phosphorylated by PINK1 to activate parkin. *Nature* **510**,
546 162–6 (2014).
- 547 15. Pickrell, A. M. & Youle, R. J. The Roles of PINK1, Parkin, and Mitochondrial Fidelity
548 in Parkinson’s Disease. *Neuron* **85**, 257–273 (2015).
- 549 16. Yamano, K. *et al.* Endosomal Rab cycles regulate Parkin-mediated mitophagy. *Elife* **7**,
550 (2018).
- 551 17. McWilliams, T. G. *et al.* Basal Mitophagy Occurs Independently of PINK1 in Mouse
552 Tissues of High Metabolic Demand. *Cell Metab.* (2018)
553 doi:10.1016/j.cmet.2017.12.008.
- 554 18. McWilliams, T. G. *et al.* Phosphorylation of Parkin at serine 65 is essential for its
555 activation in vivo. *Open Biol.* **8**, 180108 (2018).
- 556 19. Lee, J. J. *et al.* Basal mitophagy is widespread in Drosophila but minimally affected by
557 loss of Pink1 or parkin. *J. Cell Biol.* **217**, 1613–1622 (2018).
- 558 20. McWilliams, T. G. *et al.* *mito*-QC illuminates mitophagy and mitochondrial
559 architecture in vivo. *J. Cell Biol.* **214**, 333–345 (2016).
- 560 21. McWilliams, T. G. *et al.* A comparative map of macroautophagy and mitophagy in the
561 vertebrate eye. *Autophagy* **0**, 1–13 (2019).
- 562 22. Parisiadou, L. *et al.* Phosphorylation of ezrin/radixin/moesin proteins by LRRK2
563 promotes the rearrangement of actin cytoskeleton in neuronal morphogenesis. *J.*

- 564 *Neurosci.* **29**, 13971–80 (2009).
- 565 23. Lin, X. *et al.* Leucine-rich repeat kinase 2 regulates the progression of neuropathology
566 induced by Parkinson’s-disease-related mutant alpha-synuclein. *Neuron* **64**, 807–27
567 (2009).
- 568 24. Reith, A. D. *et al.* GSK2578215A; a potent and highly selective 2-arylmethoxy-5-
569 substituent-N-arylbenzamide LRRK2 kinase inhibitor. *Bioorg. Med. Chem. Lett.* **22**,
570 5625–9 (2012).
- 571 25. Fell, M. J. *et al.* MLi-2, a Potent, Selective, and Centrally Active Compound for
572 Exploring the Therapeutic Potential and Safety of LRRK2 Kinase Inhibition. *J.*
573 *Pharmacol. Exp. Ther.* **355**, 397–409 (2015).
- 574 26. Montava-Garriga, L., Singh, F., Ball, G. & Ganley, I. G. Semi-automated quantitation
575 of mitophagy in cells and tissues. *Mech. Ageing Dev.* **185**, 111196 (2020).
- 576 27. Schindelin, J. *et al.* Fiji: an open-source platform for biological-image analysis. *Nat.*
577 *Methods* **9**, 676–682 (2012).
- 578 28. Singh, F., Ball, G. & Ganley, I. G. Semi-automated quantitation of macroautophagy
579 with the auto-QC counter. <https://www.protocols.io/> (2020)
580 doi:dx.doi.org/10.17504/protocols.io.bnzamf2e.
- 581 29. RStudio Team. RStudio: Integrated Development for R. (2015).
- 582 30. Allen, G. F. G., Toth, R., James, J. & Ganley, I. G. Loss of iron triggers PINK1/Parkin-
583 independent mitophagy. *EMBO Rep.* **14**, 1127–1135 (2013).
- 584 31. Nichols, R. J. *et al.* Substrate specificity and inhibitors of LRRK2, a protein kinase
585 mutated in Parkinson’s disease. *Biochem. J.* **424**, 47–60 (2009).
- 586 32. Ito, G. *et al.* Phos-tag analysis of Rab10 phosphorylation by LRRK2: a powerful assay
587 for assessing kinase function and inhibitors. *Biochem. J.* **473**, 2671–2685 (2016).

- 588 33. Uhlén, M. *et al.* A Human Protein Atlas for Normal and Cancer Tissues Based on
589 Antibody Proteomics. *Mol. Cell. Proteomics* **4**, 1920–1932 (2005).
- 590 34. Uhlen, M. *et al.* Towards a knowledge-based Human Protein Atlas. *Nat. Biotechnol.*
591 **28**, 1248–1250 (2010).
- 592 35. Baptista, M. A. S. *et al.* LRRK2 kinase inhibitors induce a reversible effect in the lungs
593 of non-human primates with no measurable pulmonary deficits. *bioRxiv* 390815 (2018)
594 doi:10.1101/390815.
- 595 36. Plowey, E. D., Cherra, S. J., Liu, Y.-J. & Chu, C. T. Role of autophagy in G2019S-
596 LRRK2-associated neurite shortening in differentiated SH-SY5Y cells. *J. Neurochem.*
597 **105**, 1048–56 (2008).
- 598 37. Fuji, R. N. *et al.* Effect of selective LRRK2 kinase inhibition on nonhuman primate
599 lung. *Sci. Transl. Med.* **7**, 273ra15-273ra15 (2015).
- 600 38. Schapansky, J., Nardoizzi, J. D. & LaVoie, M. J. The complex relationships between
601 microglia, alpha-synuclein, and LRRK2 in Parkinson’s disease. *Neuroscience* **302**, 74–
602 88 (2015).
- 603 39. Lee, J. J. *et al.* Basal mitophagy is widespread in Drosophila but minimally affected by
604 loss of Pink1 or parkin. *J. Cell Biol.* **217**, 1613–1622 (2018).
- 605 40. Wauters, F. *et al.* LRRK2 mutations impair depolarization-induced mitophagy through
606 inhibition of mitochondrial accumulation of RAB10. *Autophagy* **16**, 203–222 (2020).
- 607 41. Bonello, F. *et al.* LRRK2 impairs PINK1/Parkin-dependent mitophagy via its kinase
608 activity: Pathologic insights into Parkinson’s disease. *Hum. Mol. Genet.* **28**, 1645–1660
609 (2019).
- 610 42. Korecka, J. A. *et al.* Mitochondrial clearance and maturation of autophagosomes are
611 compromised in LRRK2 G2019S familial Parkinson’s disease patient fibroblasts. *Hum.*

- 612 *Mol. Genet.* **28**, 3232–3243 (2019).
- 613 43. Hsieh, C.-H. *et al.* Functional Impairment in Miro Degradation and Mitophagy Is a
614 Shared Feature in Familial and Sporadic Parkinson’s Disease. *Cell Stem Cell* **19**, 709
615 (2016).
- 616 44. Pfeffer, S. R. Rab GTPases: master regulators that establish the secretory and endocytic
617 pathways. *Mol. Biol. Cell* **28**, 712–715 (2017).
- 618 45. Eguchi, T. *et al.* LRRK2 and its substrate Rab GTPases are sequentially targeted onto
619 stressed lysosomes and maintain their homeostasis. *Proc. Natl. Acad. Sci.* **115**, E9115–
620 E9124 (2018).
- 621 46. Schapansky, J., Nardozi, J. D., Felizia, F. & LaVoie, M. J. Membrane recruitment of
622 endogenous LRRK2 precedes its potent regulation of autophagy. *Hum. Mol. Genet.* **23**,
623 4201–4214 (2014).
- 624 47. Härtlova, A. *et al.* LRRK2 is a negative regulator of *Mycobacterium tuberculosis*
625 phagosome maturation in macrophages. *EMBO J.* **37**, (2018).
- 626 48. Gómez-Suaga, P. *et al.* Leucine-rich repeat kinase 2 regulates autophagy through a
627 calcium-dependent pathway involving NAADP. *Hum. Mol. Genet.* **21**, 511–525
628 (2012).
- 629 49. Bravo-San Pedro, J. M. *et al.* The LRRK2 G2019S mutant exacerbates basal autophagy
630 through activation of the MEK/ERK pathway. *Cell. Mol. Life Sci.* **70**, 121–136 (2013).
- 631 50. Manzoni, C. *et al.* Inhibition of LRRK2 kinase activity stimulates macroautophagy.
632 *Biochim. Biophys. Acta - Mol. Cell Res.* **1833**, 2900–2910 (2013).
- 633 51. Orenstein, S. J. *et al.* Interplay of LRRK2 with chaperone-mediated autophagy. *Nat.*
634 *Neurosci.* **16**, 394–406 (2013).

635

636 **Figure legends**

637 **Figure 1. LRRK2 kinase activity impairs basal mitophagy *in vitro***

638 (A) Schematics of the *mito-QC* reporter in mouse model. (B) Representative images of *mito-*
639 *QC* primary MEF cultures established from LRRK2 WT, LRRK2 G2019S, and LRRK2 KO
640 embryos. Boxed area is magnified on the right and arrowheads indicate examples of
641 mitophagy (mCherry-only mitolysosomes). (C) Quantitation of data shown in B from 6-9
642 independent experiments. Below is representative immunoblot showing LRRK2 protein
643 expression. (D) Schematics of the *auto-QC* reporter in mouse model. (E) Representative
644 images of *auto-QC* primary MEF cultures established from LRRK2 WT, LRRK2 G2019S,
645 and LRRK2 KO embryos. Boxed area is magnified on the right and arrowheads indicate
646 examples of autolysosomes and arrows highlight autophagosomes. (F) Quantitation of data
647 shown in E from 4-6 independent experiments. (G) Representative images of *mito-QC*
648 primary MEFs treated with control (DMSO) or 100 nM GSK3357679A. Boxed area is
649 magnified on bottom left and arrowheads indicate examples of mitolysosomes. (H)
650 Quantitation of mitophagy shown in G from 3-7 independent experiments. Corresponding
651 immunoblot of indicated proteins is shown below. Scale bars, 10 μ m. Overall data is
652 represented as mean \pm SEM. Statistical significance is displayed as * p <0.05, and
653 *** p <0.001.

654 **Figure 2. Mutation of LRRK2 *in vivo* alters brain mitophagy.**

655 (A) Representative image of tyrosine hydroxylase (TH) immunolabeled dopaminergic
656 neurons within the substantia nigra pars compacta (SNpc) undergoing basal mitophagy in
657 LRRK2 WT, LRRK2 G2019S, and LRRK2 KO *mito-QC* mice. Arrowheads show examples
658 of mitolysosomes and arrows indicate mitochondria. (B) Quantitation of the number of TH

659 positive cells per field of view using a 63x objective. (C) Quantitation of basal mitophagy per
660 μm^2 of TH staining, data points represent means from individual mice. (D) Representative
661 maximal intensity projection and isosurface render of calbindin immunolabeled Purkinje
662 neurons in *mito*-QC cerebellum sections, undergoing basal mitophagy. (E) Quantitation of
663 basal mitophagy per μm^2 of calbindin staining, data points represent means from individual
664 mice. (F) Representative image and isosurface renders of Iba1 immunolabeled microglia
665 undergoing basal mitophagy in cortical sections from LRRK2 WT, LRRK2 G2019S, and
666 LRRK2 KO *mito*-QC mice. Arrowheads highlight mitolysosomes. (G) Quantitation of the
667 number of Iba-1 positive cells in the brain cortex per field of view using a 63x objective. (H)
668 Quantitation of basal mitophagy per Iba1 positive cell body, data points represent means from
669 individual mice. (I) Representative maximal intensity projection and isosurface render of
670 GFAP immunolabeled astrocytes undergoing basal mitophagy in *mito*-QC cortical sections.
671 (J) Quantitation of basal mitophagy per μm^2 of GFAP staining, data points represent means
672 from individual mice. Scale bars, 10 μm . Overall data is represented as mean +/- SEM.
673 Statistical significance is displayed as ** $p < 0.01$, and *** $p < 0.001$.

674 **Figure 3. Effects of mutation of LRRK2 *in vivo* on basal mitophagy and**
675 **macroautophagy in selected peripheral tissues**

676 (A) Representative tile scan and images of *mito*-QC lungs from LRRK2 WT, LRRK2
677 G2019S, and LRRK2 KO mice. Arrows on the tile scan highlight Type II pneumocytes (II.),
678 alv. show alveoli. Arrowheads in the higher magnification images indicate examples of
679 mitolysosomes and circled cells correspond to Type II pneumocytes (II.) while I. indicates
680 Type I pneumocytes. (B) Quantitation of lung basal mitophagy from data shown in D, data
681 points represent means from individual mice. (C) Representative images of *mito*-QC kidney
682 cortex from LRRK2 WT, LRRK2 G2019S, and LRRK2 KO mice. glm. indicates glomeruli
683 and pt. indicates proximal tubule examples. (D) Quantitation of kidney basal mitophagy from

684 data shown in F, data points represent means from individual mice. (E) Representative
685 images of *auto*-QC lungs from LRRK2 WT, LRRK2 G2019S, and LRRK2 KO mice.
686 Arrowheads highlight autolysosomes, arrows indicate autophagosomes, and II. indicates Type
687 II pneumocytes. (F) Quantitation of lung autophagy from data shown in C, data points
688 represent means from individual mice. (G) Representative images of *auto*-QC kidney cortex
689 from LRRK2 WT, LRRK2 G2019S, and LRRK2 KO mice. Arrowheads and, arrows as in C,
690 glm. indicates glomeruli, and pt. indicates proximal tubules. (H) Quantitation of kidney
691 autophagy from data shown in E, data points represent means from individual mice. Scale
692 bars, Tile scan in A: 100 μ m, Other pictures:10 μ m. Overall data is represented as mean +/-
693 SEM. Statistical significance is displayed as **p<0.01, and ***p<0.001.

694 **Figure 4. Pharmacological rescue of LRRK2-mediated mitophagy defects *in vivo*.**

695 (A) Immunoblots of the indicated proteins from tissue lysates of LRRK2 WT, LRRK2
696 G2019S, and LRRK2 KO *mito*-QC mice treated with vehicle or GSK3357679A. (B)
697 Quantitation of phosphorylation data from A (C) Representative image of tyrosine
698 hydroxylase (TH) immunolabeled dopaminergic neurons of the substantia nigra pars
699 compacta in LRRK2 WT, LRRK2 G2019S, and LRRK2 KO *mito*-QC mice treated or not
700 (vehicle) with GSK3357679A. Arrowheads indicate mitolysosome examples. (D)
701 Quantitation of mitophagy from data shown in C, with the addition of LRRK2 KO. Each data
702 point represents mean value from an individual mouse. (E) Representative images of Iba1
703 positive cortical microglia from LRRK2 WT, and LRRK2 G2019S mice treated or not
704 (vehicle) with GSK3357679A. Arrowheads indicate mitolysosomes. (F) Quantitation of
705 mitophagy from data shown in E, with the addition of LRRK2 KO. (G) Representative
706 images of *mito*-QC lungs from LRRK2 WT, and LRRK2 G2019S mice treated or not
707 (vehicle) with GSK3357679A. Arrowheads highlight mitolysosomes. (H) Quantitation of
708 mitophagy from data shown in G, with the addition of LRRK2 KO. For (B), (D), (F), and (H),

709 V = vehicle dosed animals, GSK = GSK3357679A dosed animals. Each data point represents
710 mean value from an individual mouse. Scale bars, 10 μ m. Overall data is represented as mean
711 +/- SEM. Statistical significance is displayed as * $p < 0.05$, ** $p < 0.01$, *** $p < 0.001$, and
712 **** $p < 0.0001$.

713 **Figure S1. Stimulated mitophagy and autophagy are unchanged in MEFs**

714 (A) Representative images of WT *mito*-QC primary MEF cultures treated with control (CTL)
715 or 1mM deferiprone (DFP) for 24 h to stimulate mitophagy. Arrowheads indicate mitophagy
716 (mCherry-only mitolysosomes). (B) Quantitation of basal (CTL) and stimulated (DFP)
717 mitophagy in LRRK2 WT, LRRK2 G2019S, and LRRK2 KO *mito*-QC primary MEFs from
718 3-9 independent experiments. (C) Quantitation of *auto*-QC primary MEF cultures in basal
719 (control) and amino acid starvation (EBSS) conditions from 4-6 independent experiments. (D)
720 Quantitation of mitophagy in *mito*-QC MEFs, from 3-15 independent experiments treated
721 with increasing concentrations of GSK2578215A and MLI-2. Data is represented as mean +/-
722 SEM. Statistical significance is displayed as *** $p < 0.001$. (E) Representative immunoblots
723 MEFs treated as in D. Scale bars, 10 μ m. Overall data is represented as mean +/- SEM.
724 Statistical significance is displayed as *** $p < 0.001$.

725

726 **Figure S2. Macroautophagy in the brain is unaltered by *LRRK2* genotype.**

727 (A) Representative image of tyrosine hydroxylase (TH) immunolabeled dopaminergic
728 neurons in substantia nigra pars compacta WT *auto*-QC sections. Arrowheads indicate
729 autolysosome examples. (B) Quantitation of the number of autolysosomes (left) or
730 autophagosomes (right) per TH area in LRRK2 WT, LRRK2 G2019S, and LRRK2 KO *auto*-
731 QC mice. Data points are means from individual mice. (C) Representative image of Iba1
732 immunolabeled microglia in cortical WT *auto*-QC sections. Arrowheads indicate

733 autolysosome examples. **(D)** Quantitation of the number of autolysosomes (left) or
734 autophagosomes (right) per Iba1 positive cell in LRRK2 WT, LRRK2 G2019S, and LRRK2
735 KO *auto-QC* mice. Data points are means from individual mice. Scale bars, 10 μ m. Overall
736 data is represented as mean +/- SEM.

737 **Figure S3. Macroautophagy in the lungs and kidney cortex is not changed by LRRK2**
738 **genotype.**

739 **(A)** Quantitation of mitochondrial content, based on total *mito-QC* reporter staining, from
740 lung sections of indicated mice. Data points are means from individual animals. **(B)** Filipin
741 staining of cholesterol in type II pneumocytes within *mito-QC* lungs. Note increased staining
742 in KO. **(C)** Quantitation of basal number of autophagosomes in *auto-QC* lungs from LRRK2
743 WT, LRRK2 G2019S, and LRRK2 KO mice. **(D)** Quantitation of basal number of
744 autophagosomes *auto-QC* kidney cortex from LRRK2 WT, LRRK2 G2019S, and LRRK2
745 KO mice. Scale bars, 10 μ m. Data is represented as mean +/- SEM. Statistical significance is
746 displayed as ** $p < 0.01$.

747 **Figure S4. Pharmacological inhibition of LRRK2 kinase activity *in vitro* and *in vivo*.**

748 **(A)** Body weights of mice treated over 36 hours with vehicle (V) or GSK3357679A (X). **(B)**
749 Quantitation of Iba-1 positive cells in the brain cortex per field of view (using a 63x
750 objective) in LRRK2 WT, LRRK2 G2019S, and LRRK2 KO *mito-QC* mice treated with
751 vehicle or GSK3357679A. **(C)** Representative images of *mito-QC* kidney cortex from LRRK2
752 WT mice treated with vehicle or GSK3357679A. **(D)** Quantitation of mitophagy from data
753 shown in B. Data points represent the mean value from individual mice. Scale bars, 10 μ m.
754 Overall data is represented as mean +/- SEM. Statistical significance is displayed as
755 *** $p < 0.001$ and **** $p < 0.0001$.

756

FIGURE 1

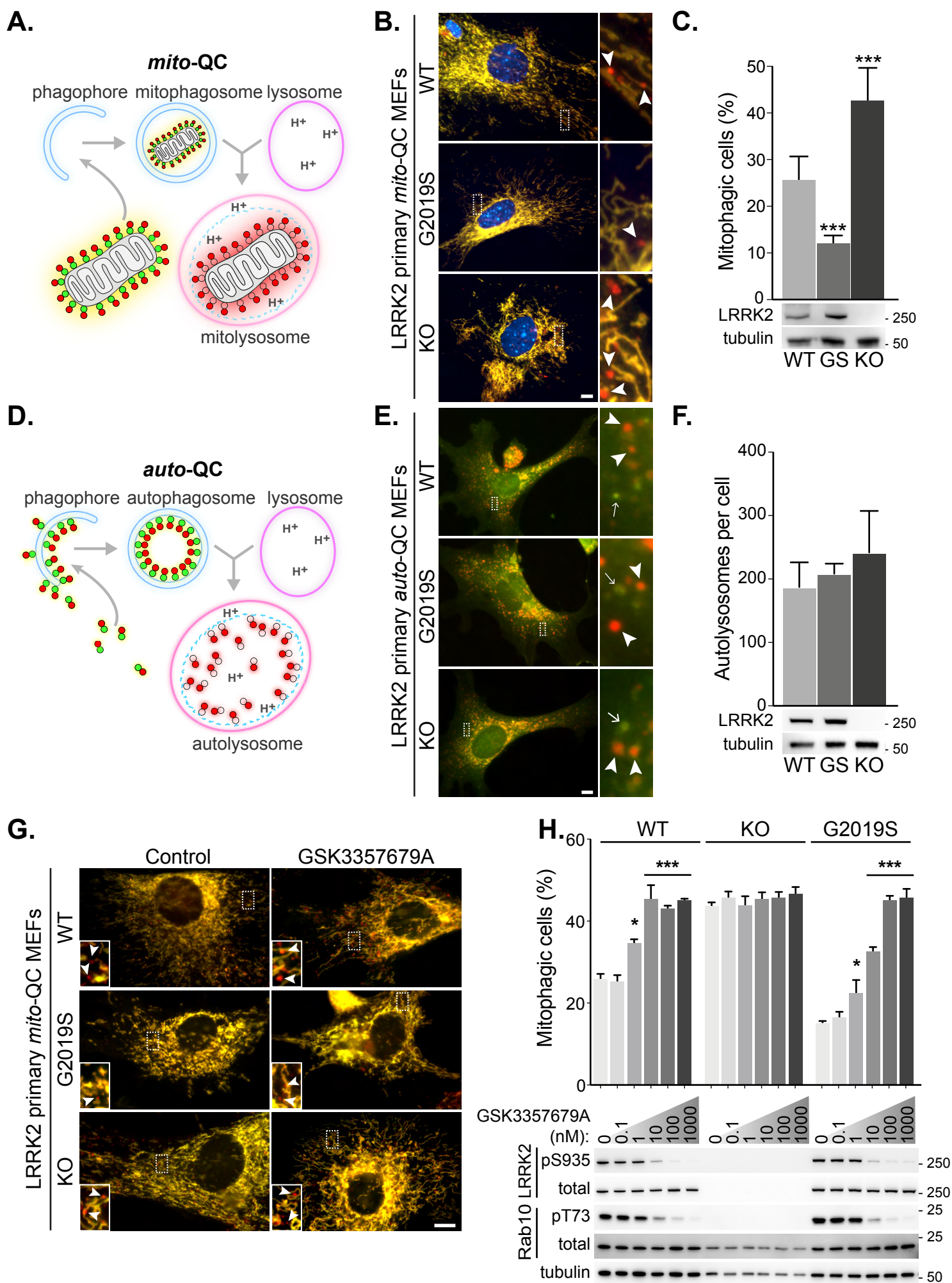
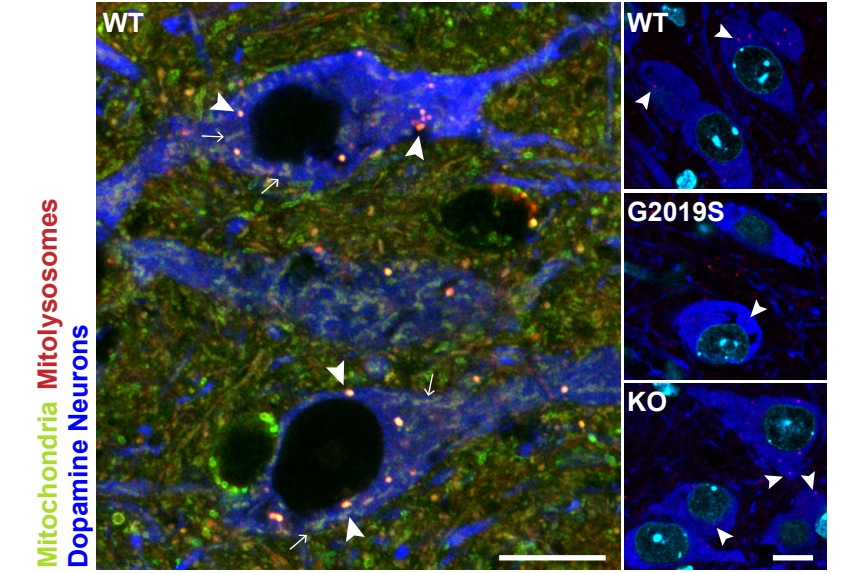
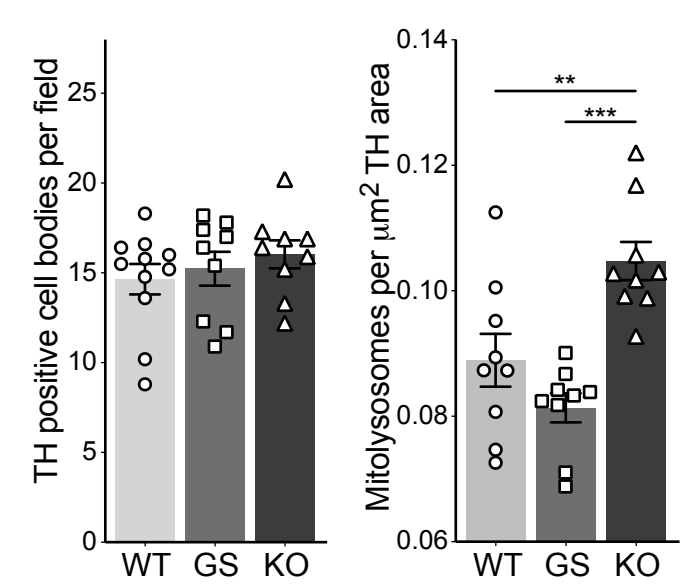


FIGURE 2

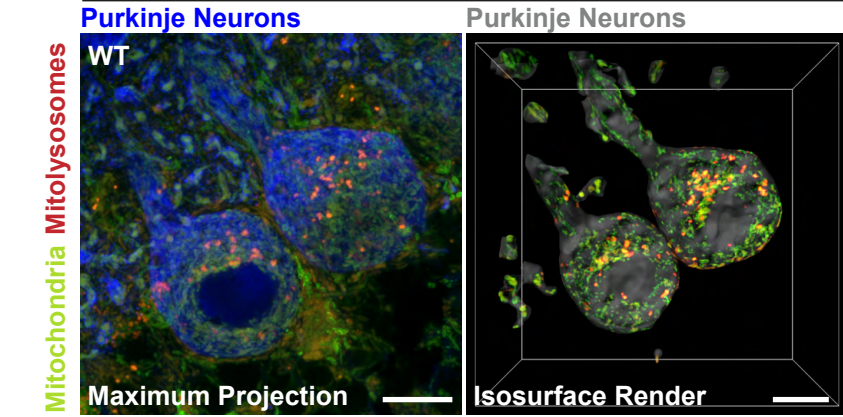
A. LRRK2 *mito-QC* Substantia nigra



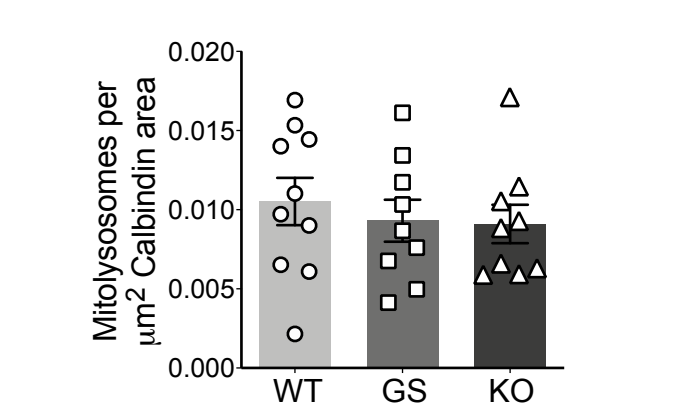
B. **C.**



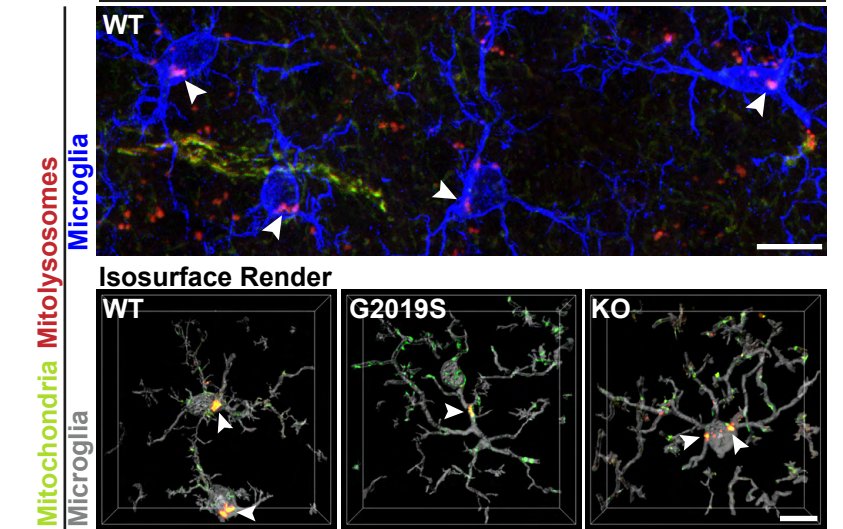
D. LRRK2 *mito-QC* Cerebellum



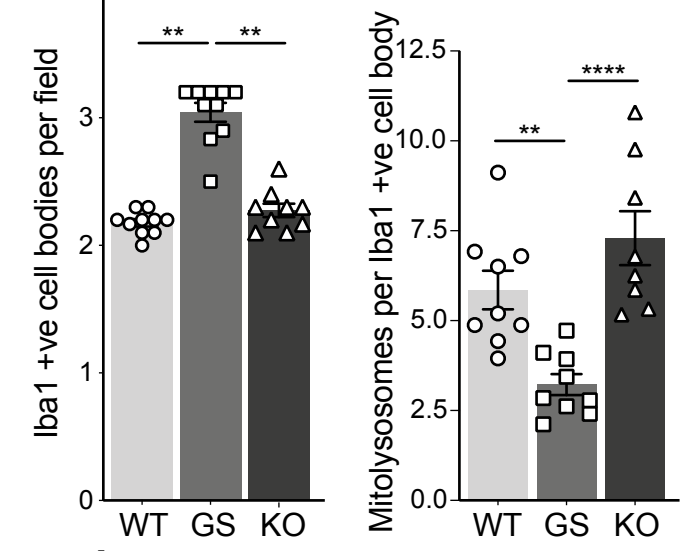
E.



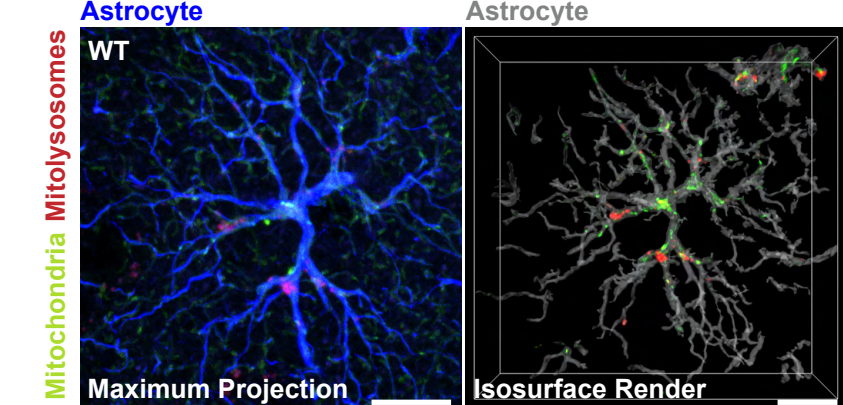
F. LRRK2 *mito-QC* Cortex



G. **H.**



I. LRRK2 *mito-QC* Cortex



J.

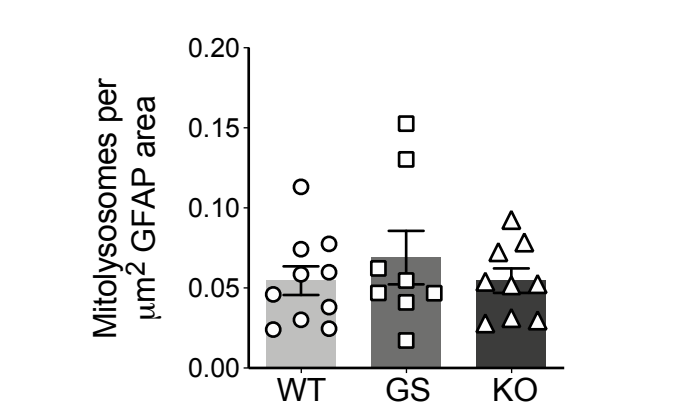
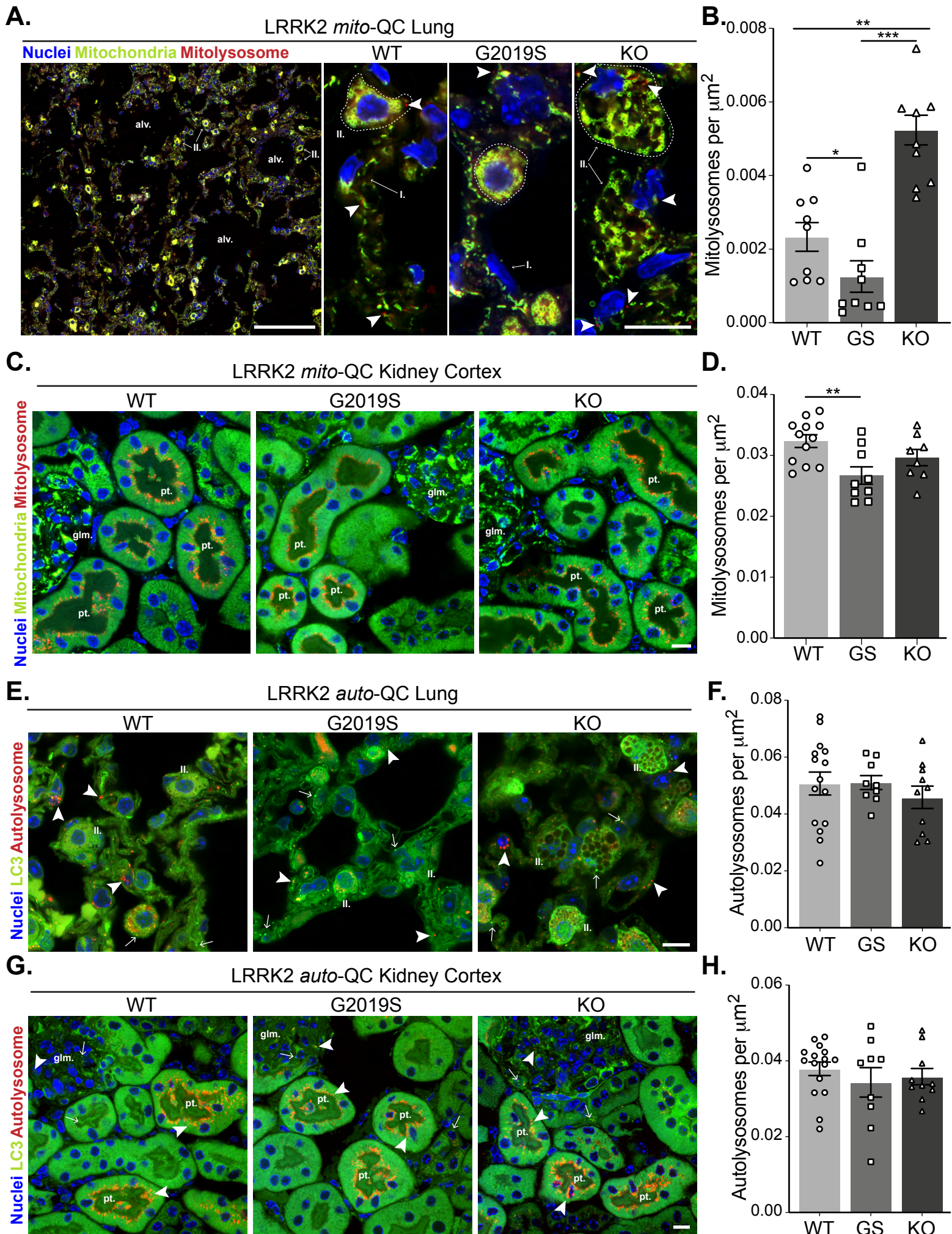
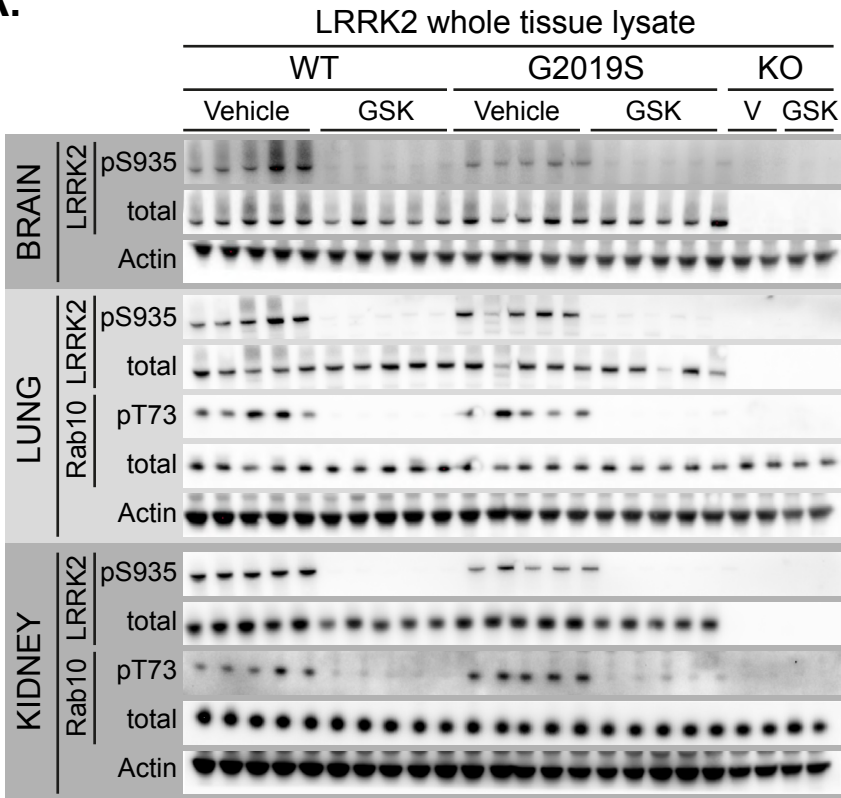


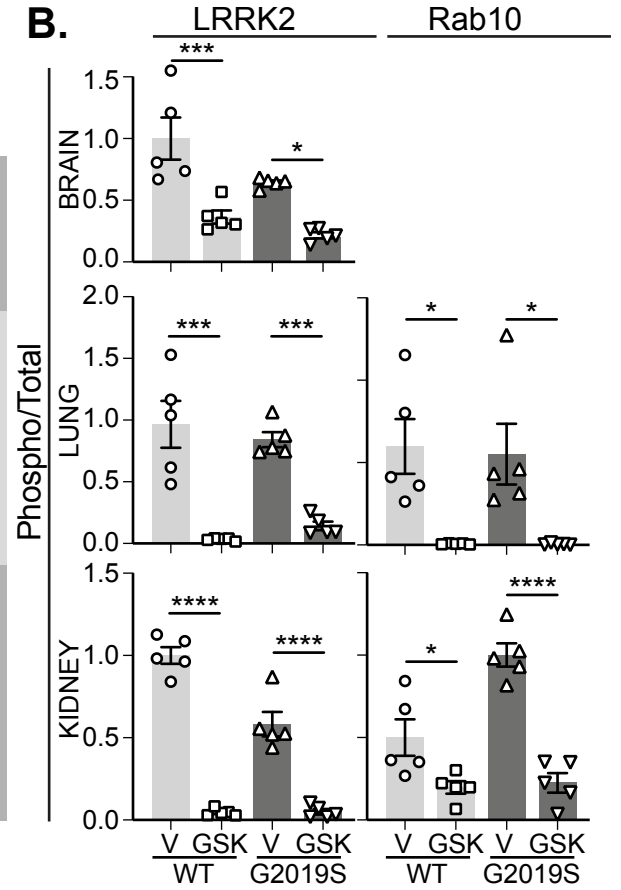
FIGURE 3



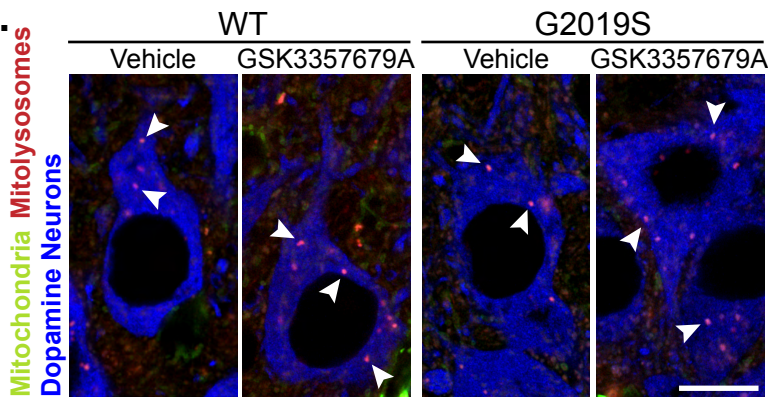
A.



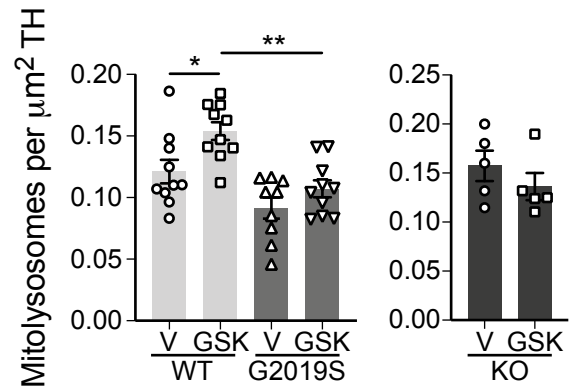
B.



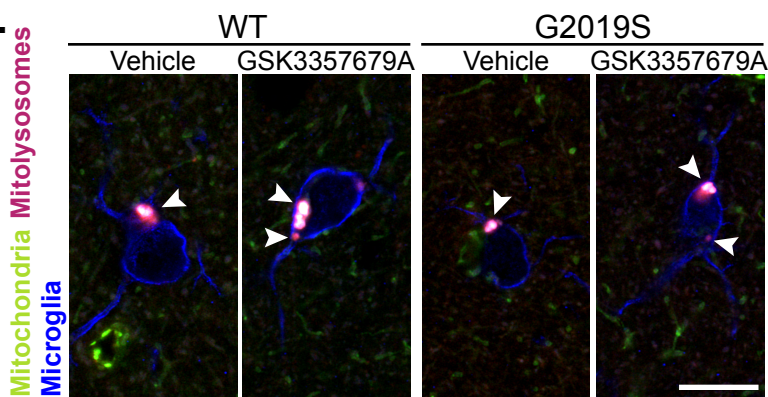
C.



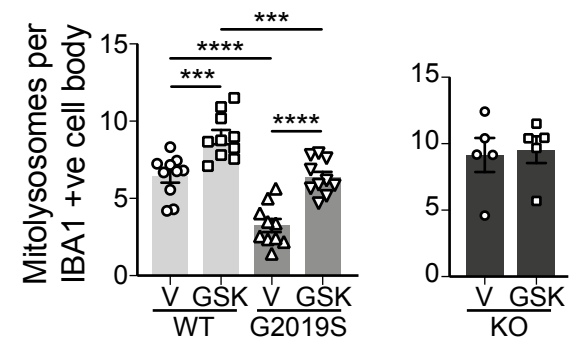
D.



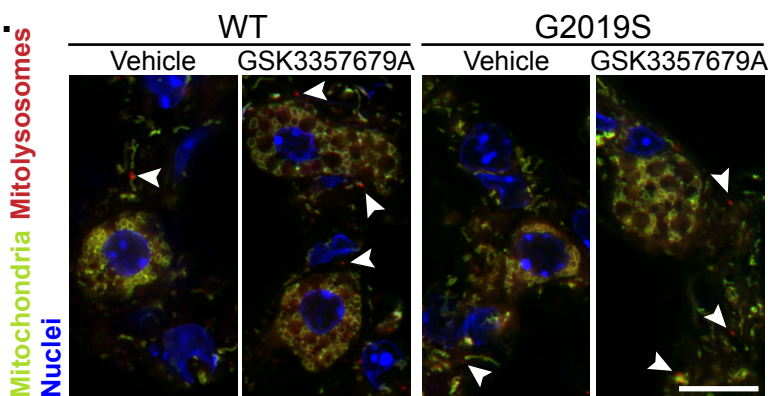
E.



F.



G.



H.

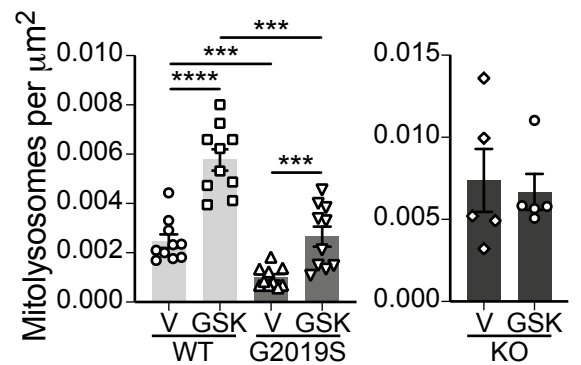
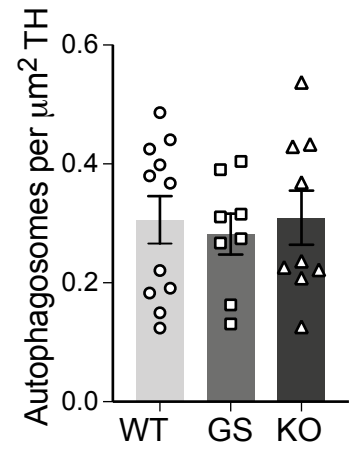
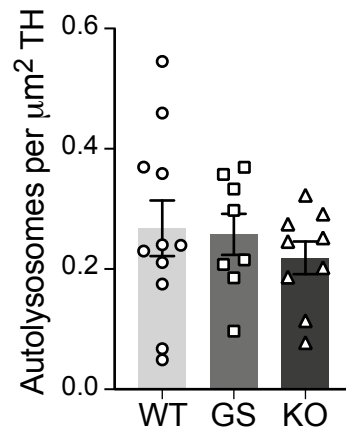
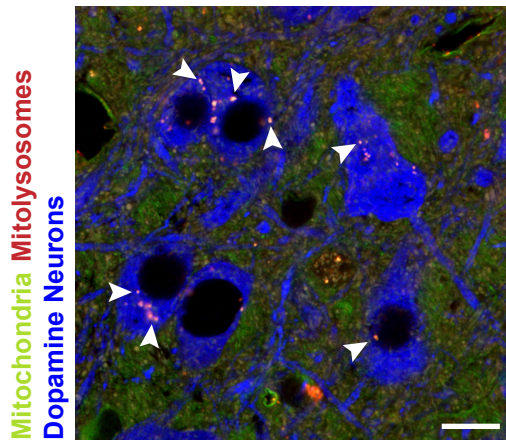
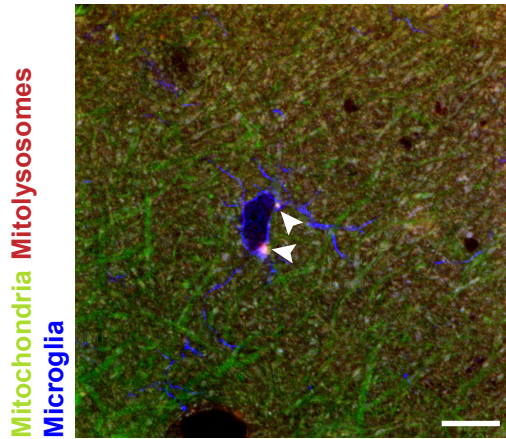


FIGURE S2

A. LRRK2 *auto*-QC Substantia nigra B.



C. LRRK2 *auto*-QC Cortex



D.

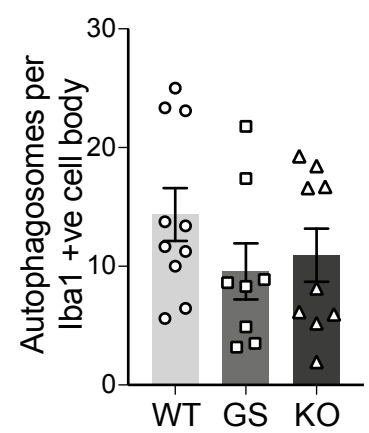
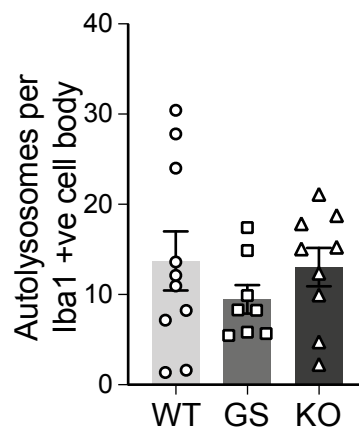
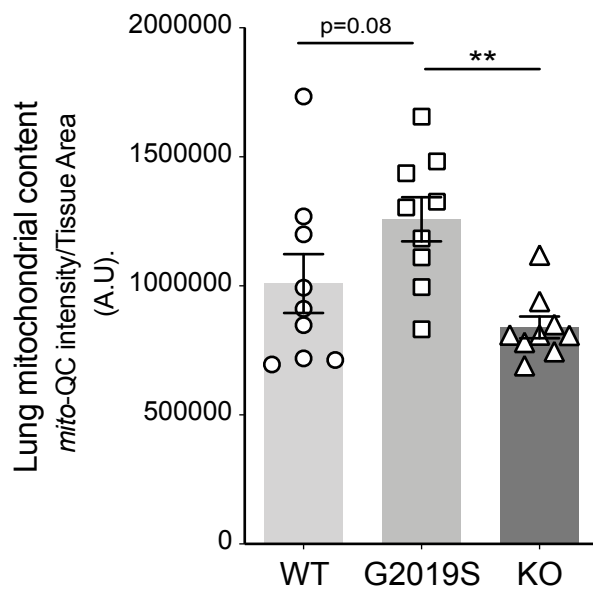


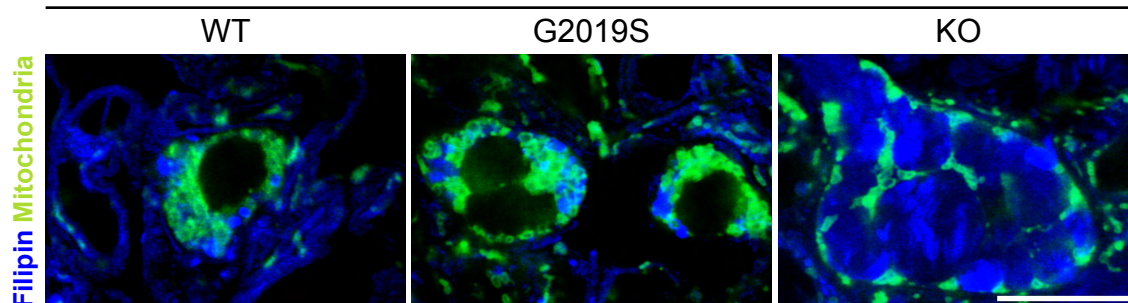
FIGURE S3

A.

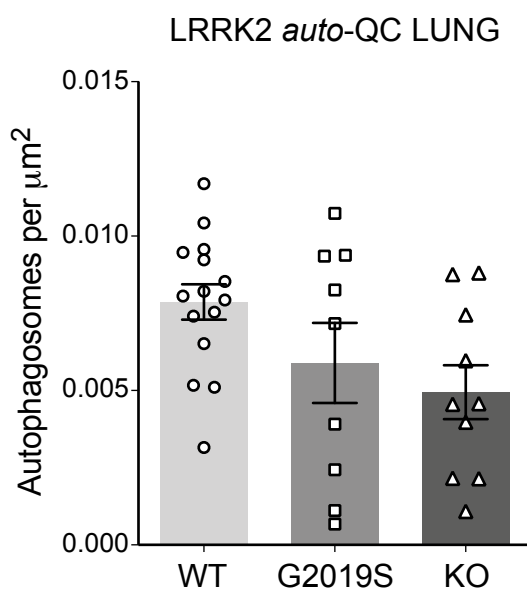


B.

LRRK2 *mito-QC* Lung: Type II Pneumocytes



C.



D.

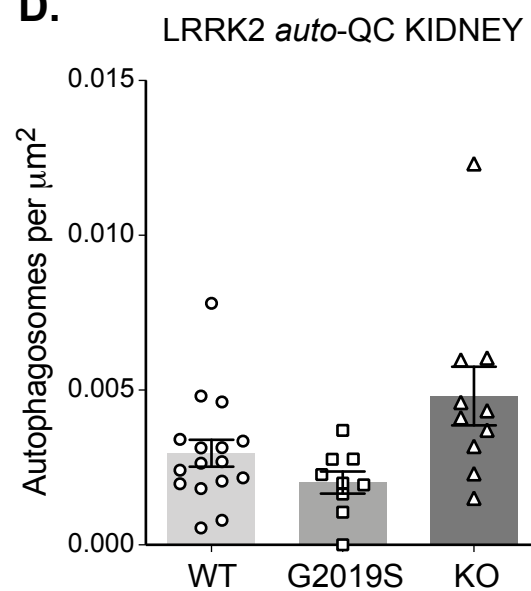


FIGURE S4

